Structural and electrical characterizations of cerium (Ce^{3+})-doped double perovskite system Sr$_2$NiMoO$_{6-\delta}$

Pravin Kumar[1] · Nitish Kumar Singh[1] · A. S. K. Sinha[2] · Prabhakar Singh[1]

Abstract The double perovskite system Sr$_{2-x}$Ce$_x$NiMoO$_{6-\delta}$ (SCNM) with $0.01 \leq x \leq 0.05$ was synthesized by the citrate–nitrate auto-combustion synthesis route. Thermal studies were carried out by simultaneous differential scanning calorimetry and thermal gravimetry. Phase constitution was analyzed by powder X-ray diffraction (XRD). Rietveld refinement showed that the major phase exists in tetragonal form with space group I4/m. Microstructural investigations revealed the formation of uniform grains. The electrical conductivity studied by impedance spectroscopy in the temperature range 300–600 °C was found to follow a thermally activated process. The sample with $x = 0.01$ showed the highest conductivity with lowest activation energy. The electrical conductivity of the system was discussed in terms of identified impurity phases and charge density $\left[Mo^{5+}_{Mo^{6+}}{}' \right]$. The variation of electrical conductivity with composition was explained on the basis of X-ray photoelectron spectroscopy and XRD studies.

1 Introduction

Double perovskite is a complex system that consists of two unit cells of perovskite structure in the form of rock salt-type ordering [1, 2]. It is represented by the general formula A$_2$BB'O$_6$ which has double-layered perovskite structures ABO$_3$ and AB'O$_3$, where A is an alkaline earth element (A = Sr, Ca, Ba), B is 3d transition metal (B = Fe, Co, Ni, Cr, etc.), and B' is a 4d transition metal (B' = Mo, Re, Sb, W, etc.) [3–6]. It contains two types of octahedral, viz BO$_6$ and B'O$_6$. Their orientations in three dimensions of crystal lattice are important to determine the physical behavior of double perovskite system [7, 8]. The various combinations of B and B' have been intensely studied for its magnetic [9], electrical [4] and optical [10] properties. In the series of advanced functional materials, double perovskite family has been suggested for technological interest, because of its high activities as ferroelectric, piezoelectric and electrode materials for SOFC [7, 11–14].

In view of excellent electrical conductivity, a few double perovskite materials were investigated with the substitution of isovalent and aliovalent cations. Influence of doping of isovalent and aliovalent cations at A, B and B' sites of A$_2$BB'O$_6$ has been found to show improved electrical conductivity [15]. In these materials, Mo-based double perovskite ceramics have represented better electrical conductivity in the growth of renewable energy technologies [14]. Recently, some materials of this class such as Sr$_2$MMoO$_6$ (M = Mg, Mn, Fe, Co, Ni, Zn, etc.) are appreciated due to their high electrical conductivity in different environments (air/H$_2$/H$_2$-Ar/CH$_4$) at lower temperatures [12]. Among them, a few materials play a key role in development of novel anode materials due to good compatibility with common electrolyte materials [11, 12]. Therefore, a series of double perovskite materials are studied as a potential candidate for anode materials for SOFC [13].

It has already been reported that Ni-doped Sr$_2$Fe$_{1.5}$Mo$_{0.5}$O$_{6-\delta}$ [16, 17], Mn-doped Sr$_2$MgMoO$_{6-\delta}$ [18] and Al-doped Sr$_2$MgMoO$_6$ [19] increase the electrical conductivity

✉ Prabhakar Singh
psingh.app@iitbhu.ac.in

[1] Department of Physics, Indian Institute of Technology (BHU), Varanasi 221005, India

[2] Department of Chemical Engineering and Technology, Indian Institute of Technology (BHU), Varanasi 221005, India

along with having a good catalytic activity. A list of trivalent cation (Al^{3+}, La^{3+}, Sm^{3+}, etc.)-doped Sr_2MgMoO_6 on Sr site has renovated the electrocatalytic activity and hence the fuel oxidation and electrochemical performances [19–21]. Among them, Vasala et al. [6] observed that M = Ni represents oxygen stoichiometric and stability under oxidizing conditions. Recently, more research groups have also rediscovered doped Sr_2NiMoO_6 for its electrical conductivity and thermal stability [22–24]. Due to its better performance as mixed ionic electronic conductor (MIEC), better stability, good catalytic activity and compatibility with other cell components, Sr_2NiMoO_6 has been proposed as a suitable anode material for SOFCs [8, 22]. Therefore, Sr_2NiMoO_6 system has been optimized for high electrical conductivity, better stability and good thermal matching with LSGM electrolyte [22]. He et al. [23] reported that Ti substitution in Sr_2NiMoO_6 is responsible for good stability, and appropriate thermal expansion and its compatibility with LSGM electrolyte. The conventional Mo-based double perovskite cermets pass through high-temperature sintering process to resolve the presence of impurity phases [25]. It is also reported that some extra phase formation in Mo-based double perovskite materials is common, which affects the electrical properties of these materials. The impurities commonly observed in these materials are $SrMoO_4$, $Sr_{3-}MoO_6$, Ni and NiO [6, 23, 26–28]. Looking at the interesting properties and applications of Sr_2NiMoO_6 double perovskite systems, in the present work, we have studied the electrical conductivity of cerium-doped Sr_2NiMoO_6 double perovskite system, $Sr_{2-x}Ce_xNiMoO_6$ ($0.01 \leq x \leq 0.05$). The substitution of trivalent Ce ion on divalent Sr ion has been chosen with the motive that it will increase the reduction of Mo^{6+} into Mo^{5+}. This redox reaction will enhance the electronic conductivity leading to a mixed ionic electronic conductivity in the system.

This system has been synthesized via a citrate–nitrate auto-combustion method. Its properties were characterized by applying X-ray powder diffraction (XRD), thermogravimetric analysis/differential scanning calorimetry (TG/DSC), scanning electron microscopy (SEM), X-ray photoelectron spectroscopy (XPS) and impedance spectroscopy, respectively. In the present work, the prepared samples with $x = 0.01$, 0.02, 0.03, 0.04 and 0.05 in the system $Sr_{2-x}Ce_xNiMoO_6$ are designated as SCNM01, SCNM02, SCNM03, SCNM04 and SCNM05, respectively.

2 Experimental section

2.1 Material synthesis process

A series of compositions $Sr_{2-x}Ce_xNiMoO_{6-\delta}$ with $x = 0.01$, 0.02, 0.03, 0.04 and 0.05 were synthesized through citrate–nitrate auto-combustion route using citric acid as a fuel. The stoichiometric amount of the starting materials $Sr(NO_3)_2$ (99.9 %, Alfa Aesar), $Ni(NO_3)_2 \cdot 6H_2O$ (99 %, Alfa Aesar), $(NH_4)_6Mo_7O_{24} \cdot 4H_2O$ (99 %, Alfa Aesar), $Ce(NO_3)_3 \cdot 6H_2O$ (99.5 %, Alfa Aesar) was weighted accurately. All nitrate precursors, ammonium molybdate and citric acid were fully dissolved in distilled water to make transparent homogenous solution. These prepared solutions were mixed together. To maintain a particular value of pH, a few drops of ammonium solution were added to homogenous solution. Mixture solution was slowly evaporated at 200 °C on hot plate arranged with magnetic stirrer. During the evaporation process, solution was gelled, foamed, swelled and finally ignited itself. After ignition voluminous ash was obtained, ash was ground with the help of agate mortar and pestle; thereafter it was calcined at 900 °C in air for 12 h. The calcined samples were shaped into pellets of diameter 12 mm and thickness around 1–2 mm using hydraulic press under optimum load of ~ 80 kg/cm^2. These ceramic pellets were sintered at 1300 °C for 12 h with heating rate of 3 °C/min.

2.2 Characterizations

To get information about phase and crystal structure of the sintered samples, powder X-ray diffraction patterns were recorded using Rigaku Miniflex II desktop diffractometer with Cu-Kα radiation ($\lambda \approx 1.5406$ Å, $20° \leq 2\theta \leq 80°$ and step of $\Delta 2\theta = 0.02°$). The TG/DSC measurement for as-prepared samples was performed using Mettler Toledo TG/DSC1 STAR^e thermal analyzer in a range of 30–1000 °C with a heating/cooling rate of 10 K/min in N_2 atmospheres. The surface morphology was studied using ZEISS scanning electron microscopy (EVO-18). The XPS spectra of all samples were taken on a KRATOS (Amicus model) high-performance analytical instrument utilizing Mg target under 1.0×10^{-6} Pa pressure. To make electrode, the sintered pellets were coated on both sides with Ag paint and fired at 700 °C for 20 min. To study the electrical properties of all silver-coated samples (diameter 12 mm and thickness 1–2 mm), conductance and dielectric loss were measured by two-probe methods using Wayne Kerr (6500 P Series) LCR meter in temperature range 300–600 °C at an interval of 25 °C within available frequency range of 20 Hz to 1 MHz.

3 Results and discussion

3.1 X-ray diffraction (XRD)

The phase and crystal structure of the system $Sr_{2-x}Ce_x$-$NiMoO_{6-\delta}$ were determined by powder X-ray diffraction

technique at room temperature. Figure 1a–e shows the X-ray diffraction patterns of the system Sr$_{2-x}$Ce$_x$NiMoO$_{6-\delta}$ with $0.01 \leq x \leq 0.05$. The XRD peak profiles of the prepared samples reveal crystalline nature of the material. The observed peaks of major phase could be pointed out on the basis of double perovskite tetragonal phase Sr$_2$NiMoO$_6$ with space group *I4/m* using JCPDS card no. 15-0601. A few traces of impurities were investigated in the X-ray diffraction pattern of the system Sr$_{2-x}$Ce$_x$NiMoO$_{6-\delta}$. The impurity phases were identified as tetragonal SrMoO$_4$ phase (s. g. *I4$_1$/a*) using JCPDS card no. 85-0586 and Cubic CeO$_2$ phase (s. g. *Fm3m*) using JCPDS card no. 04-0835.
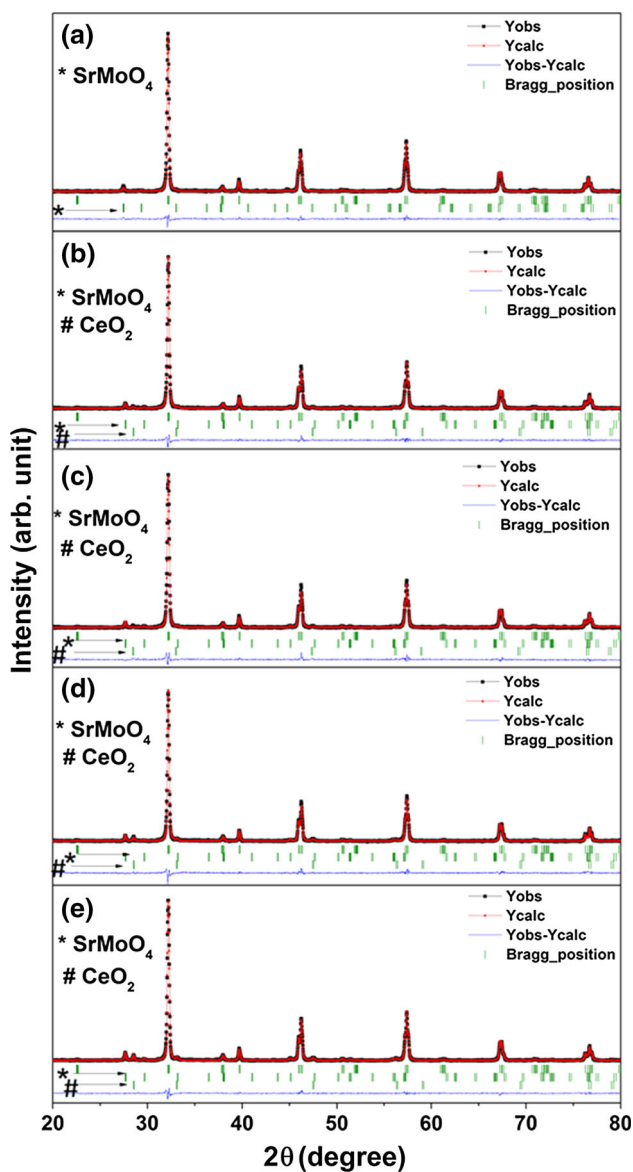

Fig. 1 Rietveld refinement of X-ray diffraction pattern of samples **a** SCNM01, **b** SCNM02, **c** SCNM03, **d** SCNM04 and **e** SCNM05. Here Yobs, Ycal and Yobs−Ycal represent the experimental data, calculated data and the difference of experimental and calculated data, respectively

In $x = 0.01$, the impurity phase SrMoO$_4$ was detected in the sample, whereas, in the samples $x = 0.02, 0.03, 0.04$ and 0.05, both phases (SrMoO$_4$ and CeO$_2$) were observed. These are indicated with asterisk symbols in Fig. 1. The average crystallite size for all powder samples was determined from the high-intense Bragg's peak corresponding to (200) reflection using Scherrer's formula

$$D = \frac{0.9\lambda}{\beta c \text{Cos}\theta} \tag{1}$$

where λ is the wavelength of X-ray, βc is corrected full width at half maxima of the diffraction peak, and θ is Bragg's diffraction angle. The average crystallite size for all compositions is given in Table 1.

The Rietveld refinement of XRD data for all SCNM-x samples is also shown in Fig. 1a–e. The refinement was carried out applying *FullProf software*, and the refined parameters of the system are mentioned in Table 1. In the refinement process, the peak profiles were modeled with pseudo-Voigt function along with the six-coefficient polynomial background. Chi-square was taken as numerical criterion for the quality of the fit between experimental and calculated diffraction patterns. The refined lattice parameter and Chi-square value of the system are given in Table 1. This table shows that the cell parameters for all the samples are almost constant except the sample SCNM01 for which it is maximum. Considering the doping of Ce^{3+} ion, which has smaller ionic radii (1.02 Å) compared to that of Sr^{2+} (1.18 Å), it is expected that the lattice parameter should decrease with the increase in dopant concentration [29]. However, in present case, no such trend is observed. This could be due to combined effect of lattice strain and impure phase [30]. The percentages of volume fractions of the SrMoO$_4$ and CeO$_2$ phases, obtained from Rietveld refinement, are given in Table 1. From Table 1, it can be inferred that there is sudden decrease in percentage of volume fraction of SrMoO$_4$ with increase of Ce^{3+} substitution from 1 to 2 mol%, and thereafter, it increases gradually with increasing substitution of Ce^{3+}. This observed change in volume fraction will be discussed in explaining the conductivity behavior in the forthcoming section.

3.2 TG/DSC analysis

The TG/DSC measurements were carried out between room temperature and 1000 °C under N$_2$ atmosphere. Figure 2 shows the typical TG/DSC curves of the sample SCNM01. During heating two steps of weight loss at 500 and 800 °C were observed. The first weight loss at 500 °C may be attributed to loss of oxygen, and the second weight loss at around 800 °C may be accounted for the formation

Table 1 Variation in lattice parameters of SCNM-x ($x = 0.01, 0.02, 0.03, 0.04$ and 0.05) system

Samples	Lattice parameters			Crystallite size (nm)	χ^2	% of volume fraction of SrMoO4	% of volume fraction of CeO_2
	a (Å)	$b = c$ (Å)	Cell volume (Å)^3				
SCNM01	5.55669	7.89812	243.869	73.52	4.64	2.74	0.00
SCNM02	5.54978	7.89498	243.166	73.29	5.42	2.00	0.56
SCNM03	5.5503	7.8963	243.251	71.02	7.97	2.96	0.86
SCNM04	5.54903	7.89498	243.100	71.98	5.38	3.37	1.51
SCNM05	5.5493	7.8950	243.128	65.81	3.79	3.81	1.79
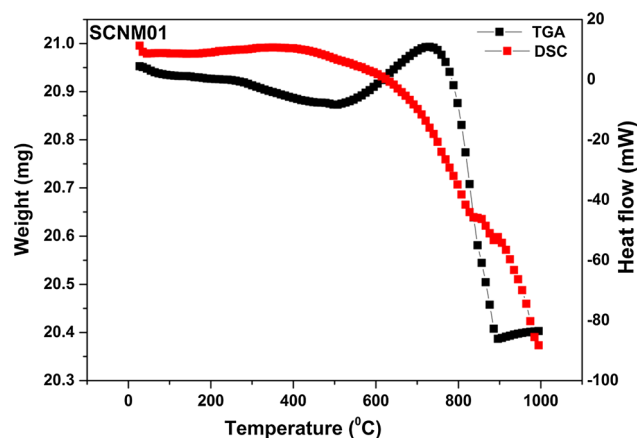
Fig. 2 TG/DSC curve for SCNM01 in N_2 atmosphere

of more oxygen vacancies under the reduction of Mo^{6+} into Mo^{5+} [8].

3.3 Scanning electron microscopy (SEM)

Scanning electron microscopy was employed to evaluate the surface morphologies of the samples. Figure 3a–e shows SEM images of conducting samples sintered at 1300 °C. The SEM images of the compositions show the formation of slightly porous materials with fine grains. The average grain size of the samples SCNM01, SCNM02, SCNM04 and SCNM05 was found approximately 5.2, 2.8, 3, 3.1 and 3.2 μm, respectively. This trend of average grain size can be correlated with the presence of impure phase in the samples. From Table 1, it can be seen that sample SCNM01 has only impure phase $SrMoO_4$, and hence, it has bigger average grain size. Whereas other samples have impure phases $SrMoO_4$ and CeO_2 and thus, these samples have smaller average grain size in comparison to SCNM01. Also the samples SCNM02, SCNM03, SCNM04 and SCNM05 have shown gradual increase in average grain size. In this regard, phase $SrMoO_4$ plays an important role to increase the average grain size, but phase CeO_2 plays inverse role. The combined effect of this two-phase result

shows the trend of the observed variation of average grain size with composition.

3.4 XPS analysis

The XPS analysis has been done to distinguish the type of charge carriers present in a particular composition of the system SCNM-x. The XPS spectrum images corresponding to Mo and O of SCNM-x samples are schematically shown in Fig. 4a, b. The XPS data have been calibrated with respect to standard C1s peak appeared at 284.6 eV. Figure 4a clearly depicts that Mo-3d spectra are split into two asymmetrical peaks corresponding to $3d_{5/2}$ and $3d_{3/2}$ states of Mo for all the compositions. These asymmetrical peaks of Mo (3d) could be fitted into two pairs of peaks and assigned to Mo^{6+} and Mo^{5+} states, respectively [27]. The XPS analysis reveals that the ratio of Mo^{5+}/Mo^{6+} is at variance with Ce^{3+} substitution on Sr^{2+} site which was determined by the ratio of the integrated area of the peaks corresponding to both states. The descriptions of the each peak for all the samples are given briefly in Table 2. The composition SCNM01 has the lowest value for the ratio of Mo^{5+}/Mo^{6+} among all the prepared samples. Figure 4b shows the peaks of O-1s core-level spectra, and these spectra have the broader and asymmetrical nature for all the samples. These peaks could be fitted into pair of peaks corresponding to two kinds of oxygen, i.e., lattice oxygen and adsorbed oxygen. The adsorbed oxygen percentages are also given in Table 2. This result depicts that the percentage of adsorbed oxygen is not consistent with Ce substitution. The absorbed oxygen generally represents the oxygen vacancies in the system which will also be responsible for reduction of Mo^{6+} into Mo^{5+}. Thus, from the above discussion, it can be inferred that the reduction of Mo^{6+} into Mo^{5+} could be attributed to two factors, i.e., actual substitution of Ce on Sr site and the oxygen vacancies present in the system. Therefore, these two factors will
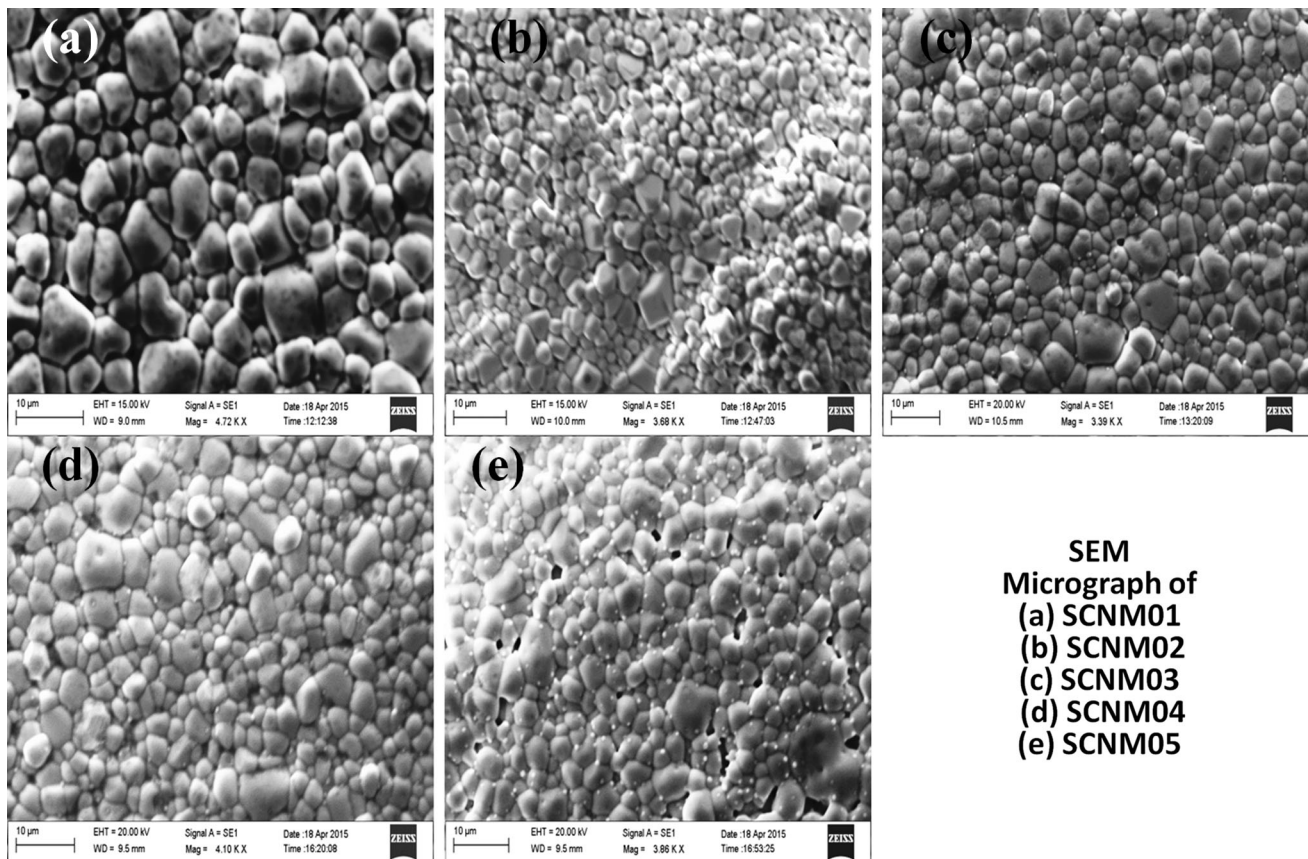
Fig. 3 Field emission scanning electron microscopy of chemically etched samples. **a** SCNM01, **b** SCNM02, **c** SCNM03, **d** SCNM04 and **e** SCNM05

control the charge carrier concentration $\left[\mathrm{Mo}^{5+}_{\mathrm{Mo}^{6+}}{}'\right]$ and hence the conduction mechanism of the system.

3.5 Electrical conductivity

The impedance spectroscopy is an important tool to understand the electrical transport property of materials and the electrochemical reactions at interfaces. The impedance spectra $Z(\omega)$ are composed of a real $Z'(\omega)$ and an imaginary parts $Z''(\omega)$ [31]. The electrical conductivity of the all prepared samples was studied applying complex-plane plot of impedance spectra. The resistance of charge transfer is calculated by depressed semicircular arc under entire frequency range (high to low) of the complex-plane plot of impedance spectra [32]. The electrochemical impedance plots consist of one or more depressed semicircles. These depressed semicircles represent the contribution of grain, grain boundary and electrode polarization [33].

As a representative, the impedance spectra for the composition SCNM01 are shown in Fig. 5a–d at a few temperatures in the entire measured frequency range.

This figure illustrates the fitted data applying nonlinear least squares fitting to the Nyquist plot of real impedance (Z') versus imaginary impedance (Z''). From the above figure, it can be seen that only one depressed semicircular arc is observed with a tail. The value of capacitance C for the above observed depressed semicircular arc was calculated using the relation $\omega RC = 1$, which holds good at the peak point of the depressed semicircular arc where R, C and ω are the resistance, capacitance and angular frequency, respectively. The value of capacitance C was found to be of order of nanofarad. This value of capacitance indicates the contribution from the grain boundaries. As a representative, the corresponding modulus spectra for the composition SCNM01 are shown in Fig. 6a–d at the temperatures where the impedance spectra are given. From the above figure it can be seen that only one depressed semicircular arc is observed with a tail. The value of capacitance for this depressed semicircular arc was also calculated in the same manner as described above and found to be of order of picofarad. This value of capacitance indicates the contribution from the grains. The observed single depressed semicircular arc in impedance spectra as
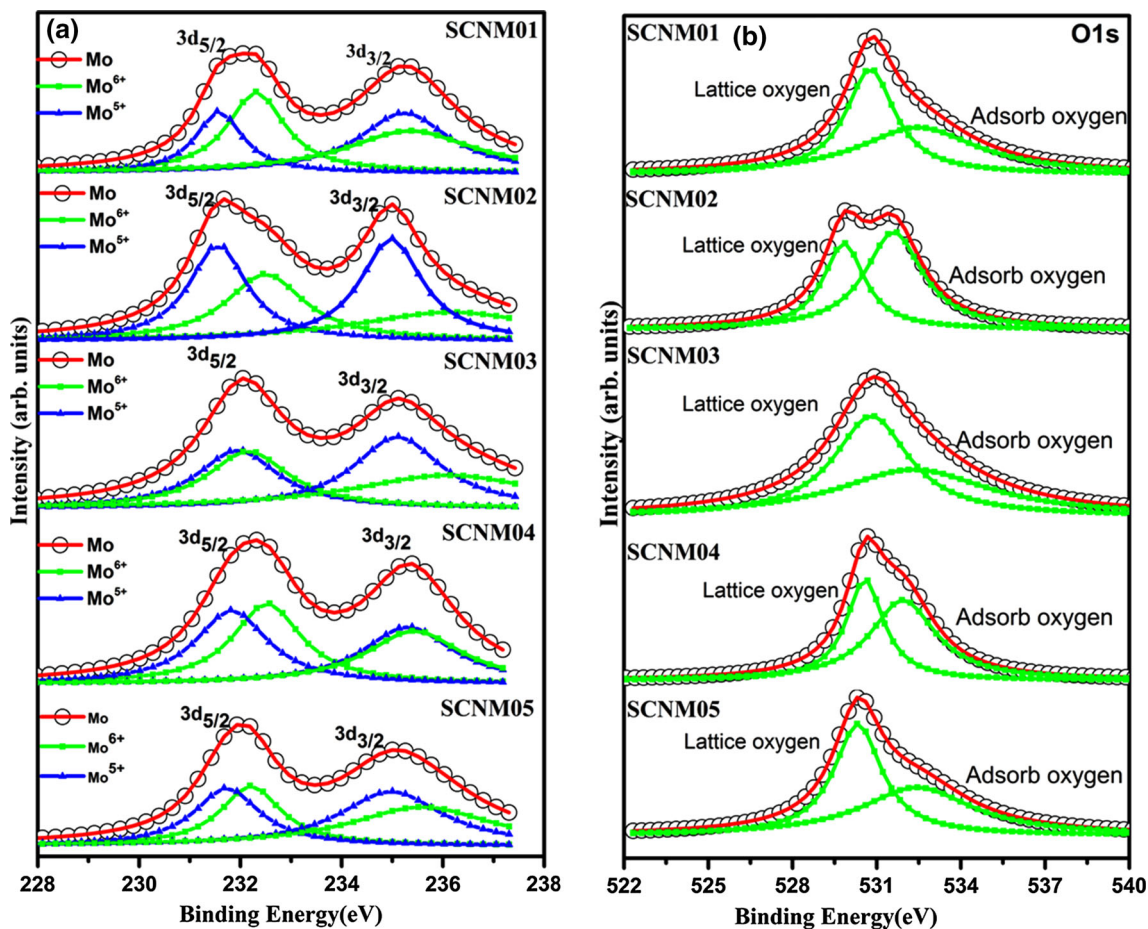
Fig. 4 XPS spectra for compositions SCNM01, SCNM02, SCNM03, SCNM04 and SCNM05: **a** Mo-3*d*, and **b** O-1*s*

Table 2 XPS fitting results of Mo-3*d* spectra and percentage of adsorbed oxygen of the system SCNM-x ($0.01 \leq x \leq 0.05$)

Compositions	Parameters	Mo^{6+}		Mo^{5+}		Mo^{5+}/Mo^{6+}	Adsorbed oxygen %
		$3d_{5/2}$	$3d_{3/2}$	$3d_{5/2}$	$3d_{3/2}$		
SCNM01	Binding energy (eV)	232.29	235.38	231.50	235.25	0.82	49.10
	Area	2544.06	2967.95	1562.17	2963.83		
SCNM02	Binding energy (eV)	232.47	235.78	231.57	235.02	1.10	54.60
	Area	1842.65	1920.74	1943.32	2230.051		
SCNM03	Binding energy (eV)	232.13	235.88	231.86	235.12	0.99	50.58
	Area	2135.97	2900.07	2138.30	2868.42		
SCNM04	Binding energy (eV)	232.60	235.42	231.84	235.44	0.98	58.18
	Area	5480.67	5251.26	5251.26	5122.57		
SCNM05	Binding energy (eV)	232.23	235.48	231.70	235.05	1.15	47.40
	Area	1831.19	2296.56	1533.14	3219.11		

well as in modulus spectra is passing through the origin. A minute analysis of both the arcs indicates that these two arcs are same and represent the combined contribution of grains and grain boundaries as the difference in the order of capacitance for both the arcs is reasonable. The reason behind this is that in impedance spectra the more resistive contribution dominates while in modulus spectra less capacitive contribution dominates [33]. Thus, impedance spectra reflect the capacitance corresponding to grain boundaries and modulus spectra reflect the capacitance corresponding to grains. The above analysis shows that each depressed semicircular arc in
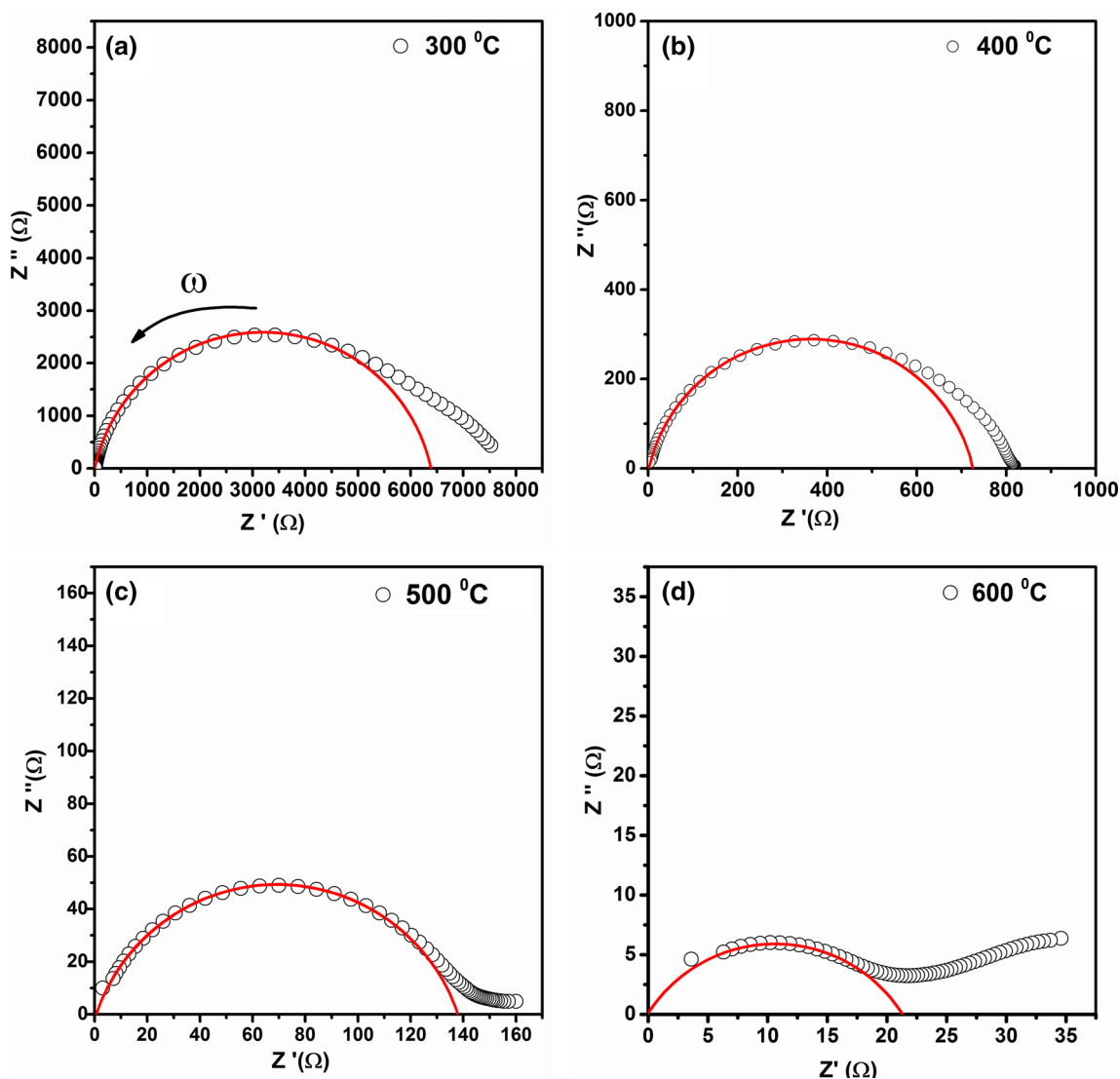
Fig. 5 Complex-plane impedance plots for the sample SCNM01 at **a** 300 °C, **b** 400 °C, **c** 500 °C and **d** 600 °C

cole–cole plot arises due to combined contributions of grain and grain boundary. Thus, the intersection of the semicircular arc on real axis (x-axis) represents the total conductivity of the system at a given temperature.

To observe the effect of doping on the impedance spectra, the cole–cole plots for all compositions at 500 °C are given in Fig. 7. For clarity, the impedance spectra for the composition SCNM01 are shown in the inset of Fig. 7. From this figure it can be concluded that the sample SCNM01 has lower impedance than that of the other samples. The value of total resistance, R_t has been obtained by the intercept of the observed depressed semicircular arc with the real axis using the Nyquist plot of real impedance (Z') versus imaginary impedance (Z''). The total conductivity of the samples was calculated using the formula

$$\sigma_t = \frac{1}{R_t} \times \frac{L}{S} \tag{2}$$

where σ_t is the total electrical conductivity, L is the thickness of pellet, R_t is the total resistance, and S is the surface area of the prepared pellets. Figure 8 shows the plots in $\log\sigma_t T$ and $1000/T$ for all samples of system SCNM-x, which represents the Arrhenius behavior. The activation energy was calculated from the slope of the above plot applying the Arrhenius relationship

$$\sigma = \frac{\sigma_0}{T} \exp\left(-\frac{E_a}{kT}\right) \tag{3}$$

where σ_0 is pre-exponential factor, E_a is the activation energy of conduction, k is the Boltzmann constant, and T is the absolute temperature. From this figure, it is clear that
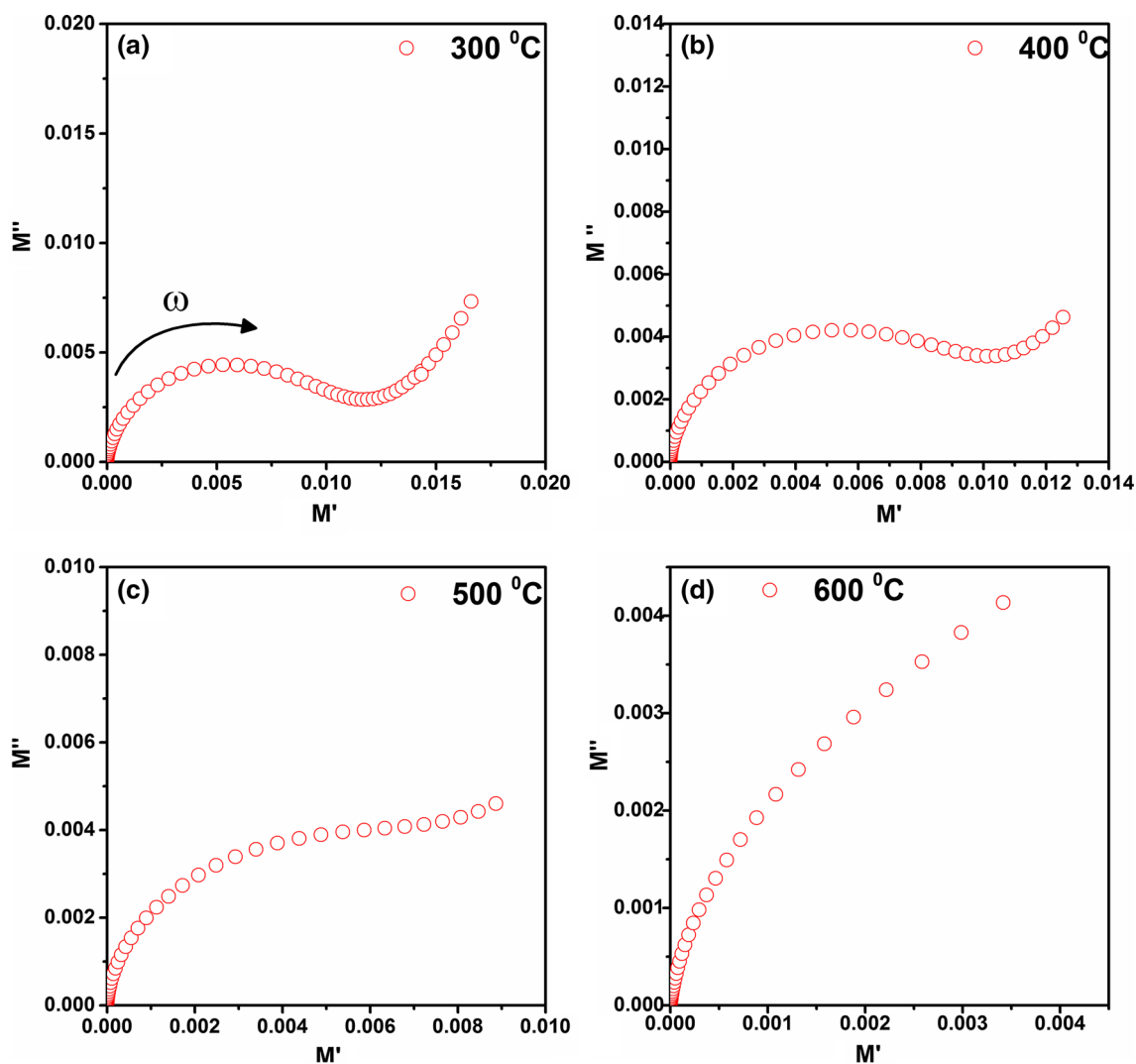
Fig. 6 Complex-plane modulus plots for the sample SCNM01 at **a** 300 °C, **b** 400 °C, **c** 500 °C and **d** 600 °C
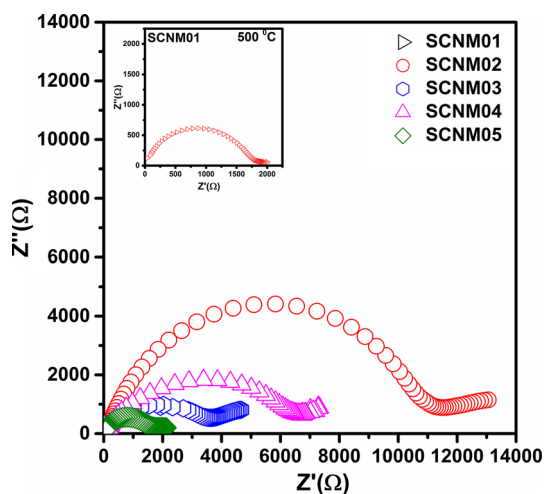

Fig. 7 Complex-plane impedance plots for samples compositions SCNM01, SCNM02, SCNM03, SCNM04 and SCNM05 at 500 °C
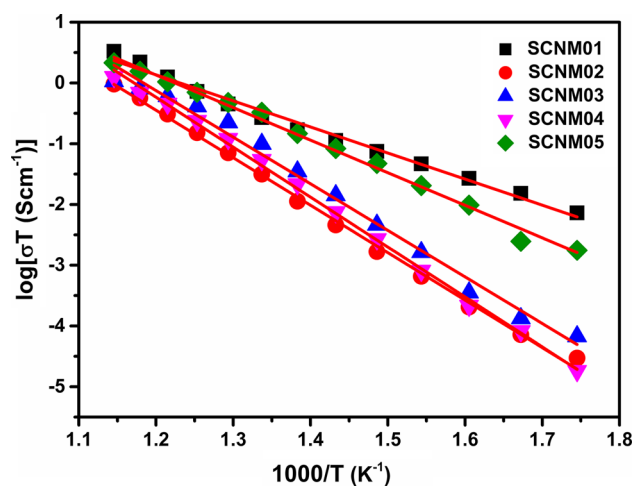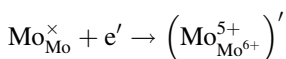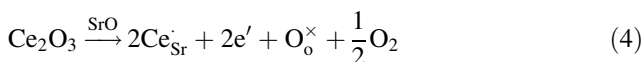
Fig. 8 Log $\sigma_t T$ versus 1000/T plots for the system SCNM-x (0.01 ≤ x ≤ 0.05)

Table 3 Activation energy of SCNM-x ($x = 0.01, 0.02, 0.03, 0.04$ and 0.05) system

Compositions	Temperature range (°C)	E_a (eV) from $\log(\sigma T)$ versus $1000/T$ plot
SCNM01	300–600	$E_a = 0.85$
SCNM02	300–600	$E_a = 1.6$
SCNM03	300–600	$E_a = 1.5$
SCNM04	300–600	$E_a = 1.6$
SCNM05	300–600	$E_a = 1.1$

the sample SCNM01 has highest electrical conductivity than the other samples. The calculated value of activation energy E_a for all samples is given in Table 3. This table also reflects the lowest activation energy for the sample SCNM01.

The electrical conductivity in system SCNM-x can be understood using defect chemistry. The doping of Ce^{3+} at Sr^{2+} site in system SCNM-x can be illustrated from the following defect equations.

$$Ce_2O_3 \xrightarrow{SrO} 2Ce_{Sr}^{\cdot} + 2e' + O_o^{\times} + \frac{1}{2}O_2 \tag{4}$$

$$Mo_{Mo}^{\times} + e' \rightarrow \left(Mo_{Mo^{6+}}^{5+}\right)'$$

Thus, the reduction of Mo^{6+} to Mo^{5+} produces electronic charge carriers, resulting in good electronic conduction and lower activation energy. For the samples with $x > 0.01$ the electrical conductivity is found to be low. This decrease in conductivity may be due to increased impurity phases. But at higher temperature more oxygen vacancy will be created due to loss of oxygen and contributed oxide ion conduction. Huang et al. [14] and Ullmann et al. [34] also reported that each oxygen vacancy reduces Mo^{6+} to Mo^{5+} which supports to increase the concentration of $\left[Mo_{Mo^{6+}}^{5+}{}'\right]$ and also increase in electronic conductivity.

4 Conclusions

Double perovskite system Sr$_{2-x}$Ce$_x$NiMoO$_{6-\delta}$ (SCNM) with $0.01 \leq x \leq 0.05$ has been prepared successfully with a few minor phases of SrMoO$_4$ and CeO$_2$. The thermal study shows the loss of oxygen at higher temperatures. Microstructural studies revealed that for 1 % doping of cerium, the grain has bigger size than that of the other samples but for the composition having 2 mol% cerium, grain size decreases and again increases for higher percentage of doping. The XPS study of all compositions predicted the reduction of Mo^{6+} into Mo^{5+}. The doping of cerium increases the electrical conductivity of the studied

system due to the production of electronic charge carriers. It seems that the doping of cerium greater than 1 mol% increases the impurity phase, which results the decrease in electrical conductivity. The sample SCNM01 has highest conductivity with lowest activation energy of 0.85 eV.

References

1. S. Tao, J. Canales-Vázquez, J.T.S. Irvine, Chem. Mater. **16**, 2309 (2004)
2. A.A. Taskin, A.N. Lavrov, Y. Ando, Appl. Phys. Lett. **86**, 091910 (2005)
3. K. Zheng, K. Swierczek, J. Eur. Ceram. Soc. **34**, 4273 (2014)
4. Q. Zhang, T. Wei, Y. Huang, J. Power Sources **198**, 59 (2012)
5. L. Zhang, Q. Zhou, Q. He, T. He, J. Power Sources **195**, 6356 (2010)
6. S. Vasala, M. Lehtimaki, Y.H. Huang, H. Yamauchi, J.B. Goodenough, M. Karppinen, J. Solid State Chem. **183**, 1007 (2010)
7. A. Prasatkhetragarn, P. Ketsuwan, S. Maensiri, R. Yimnirun, C. Huang, D.P. Cann, J. Appl. Phys. **106**, 094105-1 (2009)
8. Y. Huang, G. Liang, M. Croft, M. Lehtimaki, M. Karppinen, J.B. Goodenough, Chem. Mater. **21**, 2319 (2009)
9. M. Retuerto, J.A. Alonso, M.J. Martinez-Lopea, N. Menendez, J. Tornero, M. Garcia-Hernandez, J. Mater. Chem. **16**, 865 (2006)
10. A. Ezzahi, B. Manoun, A. Ider, L. Bih, S. Benmokhtar, M. Azrour, M. Azdouz, J.M. Igartua, P. Lazor, J. Mol. Struct. **985**, 339 (2011)
11. P.I. Cowin, C.T.G. Petit, R. Lan, J.T.S. Irvine, S. Tao, Adv. Energy Mater. **1**, 314 (2011)
12. X.M. Ge, S.H. Chan, Q.L. Liu, Q. Sun, Adv. Energy Mater. **2**, 1156 (2012)
13. S. Sengodan, S. Choi, A. Jun, T.H. Shin, Y. Ju, H.Y. Jeong, J. Shin, J.T.S. Irvine, G. Kim, Nat. Mater. **14**, 205 (2014)
14. Y. Huang, R.I. Dass, Z. Xing, J.B. Goodenough, Science **312**, 254 (2006)
15. S. Vasala, M. Lehtimäki, S.C. Haw, J.M. Chen, R.S. Liu, H. Yamauchi, M. Karppinen, Solid State Ion. **181**, 754 (2010)
16. G. Xiao, F. Chen, Electrochem. Commun. **13**, 57 (2011)
17. G. Xiao, S. Wang, Y. Lin, Z. Yang, M. Han, F. Chena, J. Electrochem. Soc. **161**(3), F305 (2014)
18. C. Li, W. Wang, N. Zhao, Y. Liu, B. He, F. Hu, C. Chen, Appl. Catal. B **102**, 78 (2011)
19. Z. Xie, H. Zhao, T. Chen, X. Zhou, Z. Du, Int. J. Hydrog. Energy **36**, 7257 (2011)
20. Y. Ji, Y.H. Huang, J.R. Ying, J.B. Goodenough, Electrochem. Commun. **9**, 1881 (2007)
21. L. Zhang, Q. Zhou, Q. He, T. He, J. Power Sources **195**, 6356 (2010)
22. T. Wei, Y. Ji, X. Meng, Y. Zhang, Electrochem. Commun. **10**, 1369 (2008)
23. B. He, Z. Wang, L. Zhao, X. Pan, X. Wu, C. Xia, J. Power Sources **241**, 627 (2013)
24. E.A. Filonova, A.S. Dmitriev, P.S. Pikalov, D.A. Medvedev, E. Yu Pikalova, Solid State Ion. **262**, 365 (2014)
25. C. Graves, B.R. Sudireddy, M. Mogensen, ECS Trans. **28**(11), 173 (2010)

26. S. Vasala, H. Yamauchi, M. Karppinen, J. Solid State Chem. **184**, 1312 (2011)
27. Z. Xie, H. Zhao, Z. Du, T. Chen, N. Chen, J. Phys. Chem. C **118**, 18853 (2014)
28. P. Kumar, N.K. Singh, R.K. Singh, P. Singh, Appl. Phys. A **121**, 635 (2015)
29. R.D. Shannon, Acta Cryst. **A32**, 751–767 (1976)
30. P. Kumar, N.K. Singh, G. Gupta, P. Singh, RSC Adv. **6**, 22094 (2016)
31. B.W. Veal, P.M. Baldo, A.P. Paulikas, J.A. Eastman, J. Electrochem. Soc. **162**(1), H47 (2015)
32. P. Agarwal, M.E. Orazem, J. Electrochem. Soc. **139**, 1917–1927 (1992)
33. I.M. Hodge, M.D. Ingram, A.R. West, J. Electroanal. Chem. **74**, 125 (1976)
34. H. Ullmann, N. Trofimenko, F. Tietz, D. Stöver, A. Ahmad-Khanlou, Solid State Ion. **138**, 79 (2000)